2D bimetallic organic framework nanosheets for high-performance wearable power source and real-time monitoring of glucose detection

Xiaoting Zha[a], Wenyao Yang[c], Liuwei Shi[a], Qi Zeng[a], Jianhua Xu[a], Yajie Yang[a, b]**

[a] School of Optoelectronic Science and Engineering, University of Electronic Science and Technology of China, Chengdu, Sichuan 610054, China

[b] Yangtze Delta Region Institute (Huzhou), University of Electronic Science and Technology of China, Huzhou, 313001, China

[c] Chongqing Engineering Research Center of New Energy Storage Devices and Applications, Chongqing University of Arts and Sciences, Chongqing, 402160, China

Corresponding authors

Yajie Yang [a, b]* Email: jj_eagle@163.com

Wenyao Yang [c]* Email: yang0220@163.com

Abstract

Diabetics often prick their fingertips to measure the glucose levels in blood. This traditional method not only causes prolonged pain but also increases the risk of infection. Hence, in this research, a non-invasive flexible glucose biosensor with high sensitivity was fabricated. Specially, the NiCo metal–organic frameworks (NiCo-MOFs) can serve as the electrode material of micro-supercapacitors and sensing material of glucose sensors. The electrochemical tests verify that the prominent sensitivity of NiCo bimetal products is 1422.2 $\mu A\ mM^{-1}\ cm^{-2}$. The micro-supercapacitor based on as-fabricated NiCo-MOFs shows a high energy density of 11.5 mWh cm^{-2} at the power density 0.26 mW cm^{-2}. In addition, as designed glucose device possesses an excellent sensitivity of 0.31 μA/μM. A flexible energy storage and glucose detection system was successfully prepared by further integrating the micro supercapacitor and glucose sensor. The smart detector can accurately and conveniently measure glucose concentration in sweat for a real-time mode. Therefore, the wearable real-time sensing device displays feasible applications in non-invasive glucose monitoring and health management.

Keywords: NiCo-MOF, wearable sensor, supercapacitor, non-invasive glucose detection

1. Introduction

Glucose, as the main nutrient and key metabolite of human cells, is of great significance to human health.[1,2] However, glucose levels in the human body must be sustained within a well-balanced range, abnormal concentration of glucose can lead to serious health hazards and even life-threatening in some cases.[3,4] Therefore, effective detection of glucose in human body is remarkable significance for the daily management and treatment of diabetic patients. Although current commercial platforms can be rapid, easy and miniaturized measure glucose level by glucose oxidase electrodes.[5] However, enzymes are sensitive to the environment and can easily be inactivated by changes in pH, temperature and humidity.[6] Moreover, frequent pricking of the fingertip to get blood not only greatly increases the feeling of pain, but also increases the risk of infection. Fortunately, the other body fluids, for instance sweat and urine, was also founded the presence of glucose, which encourages investigators to exploit the new-type bio detectors as a non-invasive alternatives to existing glucose testing platforms.[7,8] Hence, it is important to fabricate an efficient, stable, safe, wearable, noninvasive and enzyme-free electrochemical sensor for the detection of glucose levels in body fluids.

Glucose detection in non-enzymatic devices is built on the direct electrooxidation of the catalytic site of the active material at the working electrode, which constructs a response current to linearly reflect the glucose level in the fluids.[9] Hence, the electrochemical performance of the active materials anchored in the working electrode is of great significance for the detection of glucose. Metal-organic frameworks (MOFs), a kind of porous material, which composed of metal ions (clusters) and organic ligands, has prominent electrochemical stability and easily adjustable pore structure.[10] These advantages make it widely used in gas

storage,[11,12] energy storage,[13] drug delivery[14] and sensing fields.[15] Moreover, the outstanding electrochemical properties and good biocompatibility of MOFs make them a good choice for non-enzymatic electrochemical biosensor electrode materials. However, the three-dimensional geometry of most MOFs is not conducive to exposing the active sites.[16] Therefore, the ultra-thin two-dimensional MOFs nanosheets with a large number of active reaction sites can make the material have excellent electrical conductivity and faster ion mobility, thus improving the catalytic activity of the material.[17,18] The application of single-metal MOFs in electroanalytical chemistry is limited due to its poor conductivity and unitary reaction site. By contrast, the bimetallic MOFs exbibit improved glucose detection performance on account of the synergistic effect between different metal ions during the electrochemical process.[19] For instance, Li Zhang et al. prepared the CuNi/C material for glucose detection by electrodepositing Cu nanoparticles on the surface of Ni-based MOF ramification. The high sensitivity of the prepared materials shows the excellent potential of bimetallic materials in the field of catalysis.[20] However, research on bimetallic MOFs electrode materials with high electrochemical performance in non-invasive glucose detection is quite scarce.

Overall, a three-dimensional nanoflower-like bimetallic MOF composed of two-dimensional nanosheets was finely synthesized by a straightforward solvothermal method. The sensitivity of the prepared bimetallic product is 1422.2 μA mM^{-1} cm^{-2}, which indicates a good application prospect in glucose detection. A non-invasive sensor system was developed by integrating the glucose sensor with the micro-supercapacitor (MCS) on a flexible Polyethylene terephthalate (PET) substrate. In addition, the designed sensor shows significant potential in the field of non-invasive sweat glucose detection.

2. Materials and methods

2.1. Fabrication of NiCo-BTC, Co-BTC and Ni-BTC

All chemicals are directly used after purchase. NiCo-BTC nanosheets were synthesized through ordinary solvothermal approach. Briefly, 2 mmol $Co(NO_3)_2 \cdot 6H_2O$, 1 mmol $NiCl_2 \cdot 6H_2O$ and 2 mmol 1,3,5-Benzenetricarboxylic acid (H_3BTC) were successively melted in 60 mL ethanol with moderate constant magnetic stirring for 30 min to form a homogeneous mazarine solution. The prepared mixture was placed in an autoclave and heated at 150 ℃ for 14 h. After cooling down to ambient temperature, the bluish violet powders were centrifugal washed three times by ethanol to remove the impurities in the outcomes. After drying at 60 ℃, the NiCo-BTC nanosheets were ingeniously synthesized. For comparison, the Ni-BTC (using $Ni(NO_3)_2 \cdot 6H_2O$ as the metal salts) and Co-BTC were triumphantly synthesized under the same reaction condition. The schematic illustration of NiCo-BTC synthesis is displayed in Fig. 1a.

2.2. Material Characterizations

Field-emission scanning electron microscope (FESEM, Ziess Gemini and Hitachi SU8100) was used to measure the morphology of the products. The crystal structure of the samples was characterized by transmission electron microscopy (TEM, JEOL 2100) and X-ray diffract meter (XRD, RigakuD/Max-02400) with Cu Kα radiation (1.54056Å). X-ray Photoelectron Spectroscopy (XPS, United States, Thermo Scientific K-Alpha) was employed to analyze the surface constituents of the materials. The surface functional groups of products were obtained by Fourier transform infrared spectrum (FTIR, United States, Thermo Scientific Nicolet IS 10).

2.3. Electrochemical tests of the electrode

The electrochemical performances of the designed electrode were measured by the three electrodes system of electro-chemical workstation (CHI660D, Chenhua, Shanghai, China). Detailly, the designed material, Ag/AgCl and platinum disk ($\emptyset = 2$ mm) was served as working, reference and counter electrode, respectively. The electrochemical measurements were tested in 0.1 M NaOH solution. 1.5, 0.5 and 0.05 μm alumina powder was used to remove the oxidation film on the surface of glassy carbon electrodes (GCEs, $\emptyset = 3$ mm). Then, 2 mg prepared samples were dissolved in 100 μL Nafion solution and 900 μL DI water to constitute a suspension. The turbid liquid of 5 μL was dripped onto the pretreated GCEs and dried at room temperature. The work electrodes were measured by cyclic voltammetry (CV), electrochemical impedance spectroscopy (EIS) and chronoamperometry (CA) to evaluate their electrocatalytic activity. The CV and galvanostatic charge and discharge (GCD) were used to analysis the energy storage performance of as fabricated power units.

2.4. Fabrication of designed electrode system

As shown in Fig. S1, the nonenzymic glucose biosensor system was obtained by magnetron sputtering the concentric circular pattern onto the PET matrix. Briefly, the PET substrate with the size of 1×3 cm was cleaned by ultrasonic with deionized water, ethanol and acetone, respectively. Subsequently, Cr (30 nm) and Au (100 nm) layers were orderly deposited via the magnetron sputtering manufacture. As depicted in Fig. S1, the width of the outer circular electrodes and separation is 1 mm and the semidiameter of the centric electrodes is 1.5 mm, respectively. The systems can be divided into sensor arrays (red dots part) and power units (yellow dot part), as displayed in Fig. S2.

2.5. Fabrication of power units

Power units were fabricated as follow. The NiCo-BTC nanosheets were utilized as the electrode materials of supercapacitors. Briefly, the NiCo-BTC nanosheets, acetylene black and polyvinylidene fluoride (PVDF) with the mass ratio of 8:1:1 was dispersed into N, N-dimethylformamide (DMF) under continuous magnetic stirring over 24 h to form a uniform electrode slurry. Then, the prepared suspension was dropped-cast onto the areas of designed electrodes in the power units, and natural drying in the ambient environment for 2 h. PVA/KOH gel was coated onto electrode area of micro-supercapacitors (MSCs) to complete the preparation process. The structure of the MSCs is shown in Fig. S3.

The energy density (E, Wh kg^{-1}) and power density (P, W kg^{-1}) of the MSCs were acquired from the equations (1) and (2).

$$E = \frac{1}{2} C_t V^2 = \frac{I_m \int V dt}{3.6} \quad (1)$$

$$P = \frac{3600 \times E}{\Delta t} \quad (2)$$

The C_t (F g^{-1}) denotes the capacity of micro-supercapacitors, the V (V) is the working voltage, the I_m (A g^{-1}) notes to the current density used in GCD tests and the Δt represent the discharge time of MSCs.

2.6. Fabrication of glucose sensor

To obtain the glucose sensor, the viscous solution of NiCo-BTC with 2 mg ml^{-1} was successfully prepared which is consistent with sensing electrode suspension. Then 5 μL NiCo-BTC solution was covered onto the working electrode (orange part of testing area as revealed in Fig. S4) and dried at room temperature. The in-situ redox reaction method was applied to

fabricate the Ag/AgCl conference electrode. Firstly, appropriate Ag-gel was dropped-cast onto the pattern of conference electrode. The Ag/AgCl conference electrode was successfully formed after 10 μL $FeCl_3$ (0.1M) was uniformly injected to the top of Ag-gel. Subsequently, the compensation electrode was fricated by coated on corresponding pattern (Fig.S4) with NiCo-BTC suspension and insulated membrane. Finally, PVA/KOH gel was covered the working area of the glucose sensor.

2.7. Integration of flexible glucose monitoring system

To acquire the flexible glucose monitoring system, the polyethylene (PE) file was used to packaging the whole arrays except for the glucose sensing testing region. As represented in Fig. S5a and b, the integrated monitoring system can be tightly attached on the skin, indicating the wearable and elastic capability of the monitoring system.

3. Results and discussions

3.1 Structure characterization

The morphology of NiCo-BTC was measured by FESEM. As shown in Fig. 1b, abundant 2D nanosheets are interconnected to form the nanoflower structures. Co-BTC and Ni-BTC prepared by the same method show spherical and flower-like nanosheet structures, respectively (Fig. S6a and b). As depicted in Fig. 1c, the element distribution of the NiCo-BTC powder was analyzed by EDS mapping. It can be easily observed that the Ni, Co and O element are equably distributed in the surface of materials, indicating the coexistence of Ni and Co in the sample. Fig. 1d displays the TEM image of NiCo-BTC, which confirms the thin sheets and wrinkle structure of the NiCo-BTC. Obviously, the highly-opened nanosheets exposes wealthy catalytic sites and rich diffusion paths for glucose molecules and

intermediates.[21] Furthermore, the ultra-thin and interconnect characteristic of the nanosheets immensely shorten the ion transport path and efficiently accelerated the electron-transfer rate, which indicates the advanced electrocatalytic activity.[22]

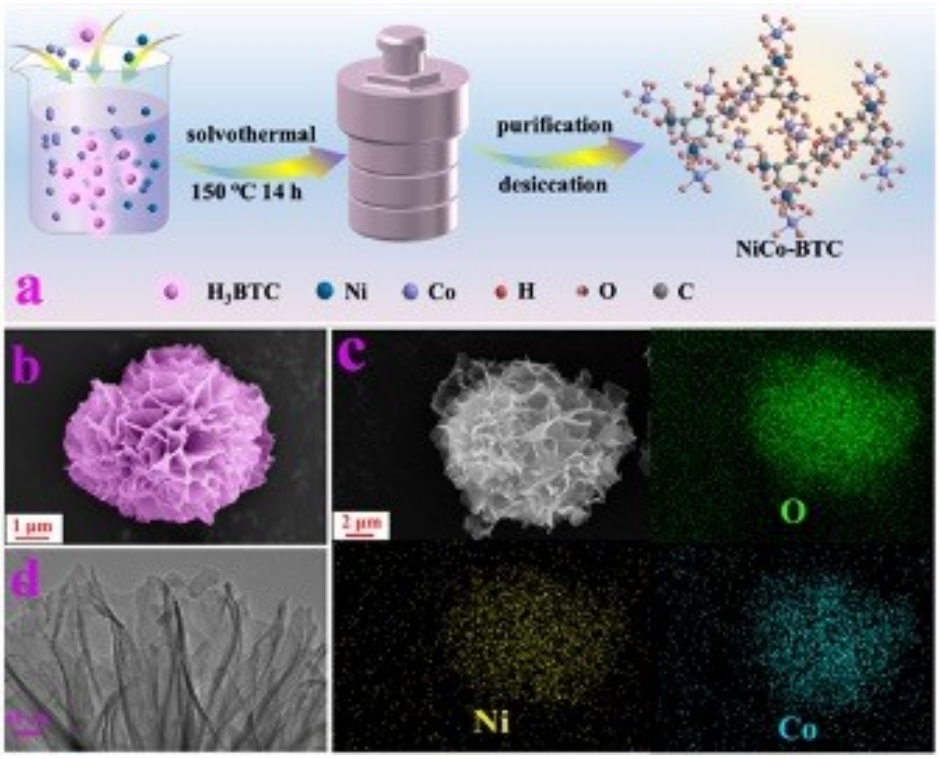

Fig. 1 (a) Synthesis illustration of NiCo-BTC, (b) SEM image of NiCo-BTC, (c) element mapping of O, Ni and Co of NiCo-BTC, (d) TEM image of NiCo-BTC.

XRD survey was employed to analyze the crystal structure of NiCo-BTC, Co-BTC and Ni-BTC. The Co-BTC has no peaks (inset of the Fig. 2a), indicating that the Co-BTC prepared by this method is amorphous, which results in the similar XRD pattern of NiCo-BTC and Ni-BTC.[23] As depicted in Fig. 2a, the characteristic diffraction peaks centered at 9.4, 13.5 and 26.7° are related to the ($\bar{2}00$), (001) and (311) planes of Ni-BTC and NiCo-BTC, which is consistent with the previous work.[24,25,26] These results demonstrate that the NiCo-BTC nanosheet has been successfully fabricated by facile solvothermal process.[23] Moreover, NiCo-BTC has poor crystallinity compared with Ni-BTC, which is due to the faster coordination

and crystallization rate of Co ions and the influence of negative ions in the reaction solution. Functional groups of the samples were characterized by FTIR measurement. The FTIR spectrum displays a sharp band at 1617 cm^{-1} and a broadband in the boundary of 3153−3556 cm^{-1} (Fig. 2b), indicating the existence of the water molecules in the inner coordination of the metallic center. It should be noted that the absorption bands at 1550 cm^{-1} is attributed to the asymmetric and symmetric vibrations of the BTC skeleton. The absorption band located at 1372 cm^{-1} results from asymmetric vibration of the NO_3^-. Moreover, the deficiency of the bands from 1690 to 1730 cm^{-1}, indexing to the −COOH groups, shows that the metal ions were successfully coordinated with the organic ligand homophonic acid.[24] Remarkably, a sharp absorption band at 721 cm^{-1} is ascribed to M-O, O-M-O and M-O-M (M=Ni, Co, and NiCo) stretching vibrations.[27] Obviously, the results of FTIR analysis were consistent with those of XRD characterization.

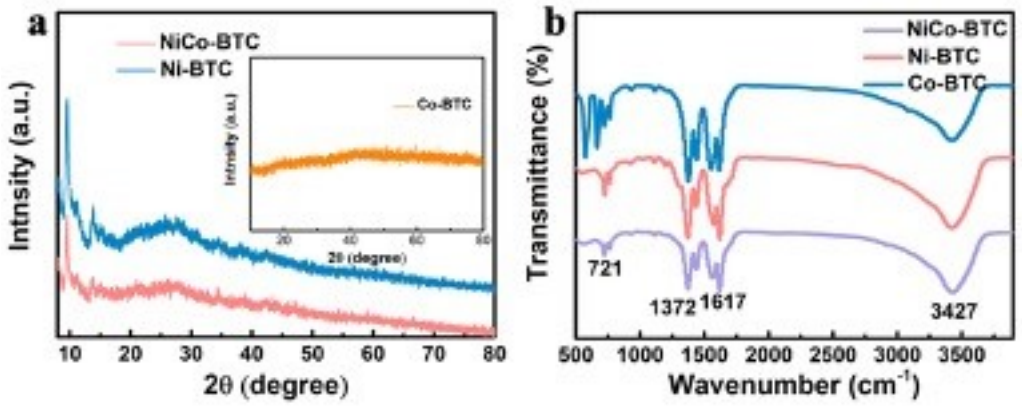

Fig. 2 The (a) XRD and (b) FTIR of samples.

XPS was characterized to illustrate the chemical states of electrocatalyst materials. The survey spectrum of bimetallic MOFs (Fig. 3a) demonstrates the coexistence of Co, C, Ni and O in NiCo-BTC, which is compliance with the EDS result. In addition, the absence of Ni in Co-BTC and Co in Ni-BTC further demonstrate the successful synthesis of the monometallic

materials. The high-definition spectrum of Ni 2p in the bimetallic composite is shown in Fig. 3b. For Ni 2p spectrum, the peaks located at 863.4 eV and 881.6 eV belongs to the satellite peaks of Ni $2p_{3/2}$ and Ni $2p_{1/2}$, respectively. It is noted that, the marked peaks at 855.7 eV and 873.3 eV are assigned to Ni^{2+}, and the peaks at 859.9 eV and 877.5 eV are attributed to Ni^{3+}. The spectrum of Ni 2p of Ni-BTC has a similar composition to NiCo-BTC, which possesses these peaks of Ni^{3+} and Ni^{2+} at the corresponding binding energy (Fig. 3c). The ratios of $Ni^{3+}/(Ni^{2+}+Ni^{3+})$ of NiCo-BTC and Ni-BTC calculated by the corresponding peak area are 57.2% and 51.7%, respectively, which indicates that the existence of Co atom significantly influences the valence of Ni. On the basis of previous literature, the high valence of Ni atom has a stronger ability to accept electrons, which is conducive to the charge transfer process between OH^- and the electrode material, resulting in a significant increase for the oxidation capacity for glucose molecules of NiCo-BTC.[28] Fig. 3d displays the high-resolution XPS (HRXPS) spectrum of Co 2p of bimetallic products. The two pairs characteristic peaks of Co $2p_{3/2}$ and Co $2p_{1/2}$ locate at 781/796.9 eV and 783.8/800.1 eV indicating the existence of Co^{3+} and Co^{2+} in the sample. The satellite peaks of Co 2p locate at 787 eV and 802.7 eV.[29] As shown in Fig. 3e, the Co 2p with Co-BTC presents the peaks of Co $2p_{3/2}$, Co $2p_{1/2}$ and satellite peaks, respectively, which is in accord with the corresponding spectrum of NiCo-BTC, manifesting the alike valence states of Co atoms in Co-BTC and NiCo-BTC. The binding energy of 284.5, 284.8 and 288.4 eV in C 1s of NiCo-BTC (Fig. 3f) are due to the characteristic spectrum of C=C, C-C and O-C=O groups, respectively.[30] These characteristic peaks can be ascribed to the BTC skeleton and the −COOM (M= Ni, Co, and NiCo). As displayed in Fig. 3g, the O 1s fitting curve generates four peaks at 530.8, 531.4, 532 and 533

eV, which can be attributed to the typical metal-oxygen binding, oxygen in the low-valence state, NO_3^- rising from the raw materials and hydroxyl deriving from the water molecules in the inner coordination sphere of the metallic center, respectively.[31] These results prove that the pure phase NiCo-BTC was successfully prepared.

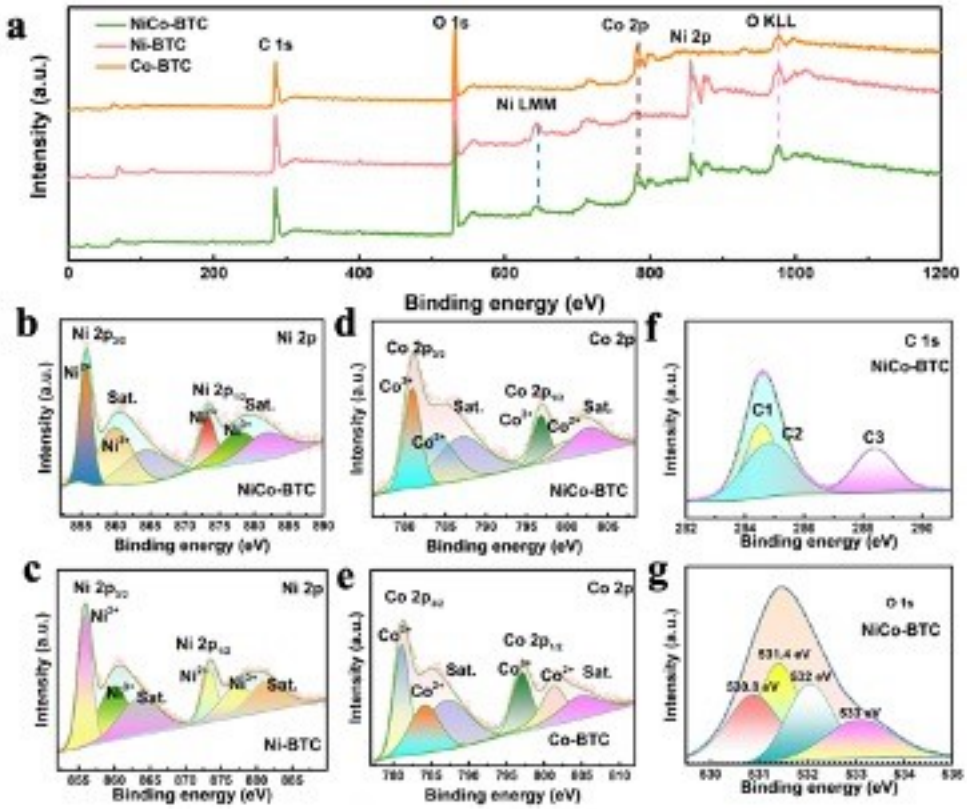

Fig. 3 XPS spectra of NiCo-BTC, Ni-BTC and Co-BTC (a) Survey of all samples, (b) Ni 2p of NiCo-BTC, (c) Ni 2p of Ni-BTC, (d) Co 2p of NiCo-BTC, (e) Co 2p of Co-BTC, (f) C 1s of NiCo-BTC, (g) O 1s of NiCo-BTC.

3.2 Glucose sensing performance of electrodes

The CV curves of NiCo-BTC, Ni-BTC and Co-BTC electrodes in the presence and absence of glucose are demonstrated in Fig. 4a, Fig. S7 and Fig. S8. When the glucose concentration ranges from 0 to 0.5 mM, the current response of Ni-BTC and Co-BTC is 8 μA and 3 μA, respectively. Whereas, the current response of Ni-BTC and Co-BTC was significantly lower

than that of NiCo-BTC (14 μA). The higher current responses and bigger area of CV curves prove the enhanced electrocatalytic activities of the bimetallic material. The reaction expressions of redox peaks in the CV curves of 0 mM are as follows:(3), (4) and (5).[24] In other words, metal ions in the electrode material react with OH^- in solution under a certain voltage to form metal ions in high valence states.

$$Ni(II) - BTC + OH_{sol}^{-} \rightleftharpoons Ni(III) - (OH)BTC + e^- \quad (3)$$

$$Co(II) - BTC + OH_{sol}^{-} \rightleftharpoons Co(III) - (OH)BTC + e^- \quad (4)$$

$$Co(III) - BTC + OH_{sol}^{-} \rightleftharpoons Co(IV) - (OH)BTC + e^- \quad (5)$$

Furthermore, Fig. S9 and Eqs. (6), (7) and (8)[24,32,33] demonstrate the electrocatalytic oxidation reactions of NiCo-BTC for glucose. Firstly, acidic hydroxyl groups in glucose interact with the electrode surface. Then, the acidic functional groups react with OH^- in the electrolyte to form intermediates. After that, the hypervalent Ni and Co react with adsorbed intermediates to form gluconolactone. The change to the oxidation state of Ni and Co and the formation of gluconolactone generate the destruction of the chemisorption bond and desorption of gluconolactone resulting the form of gluconic acid.[33]

$$2Ni(III) - (OH)BTC + C_6H_{12}O_6 \rightleftharpoons 2Ni(II) - BTC + C_6H_{10}O_6 + 2H_2O \quad (6)$$

$$2Co(III) - (OH)BTC + C_6H_{12}O_6 \rightleftharpoons 2Co(II) - BTC + C_6H_{10}O_6 + 2H_2O \quad (7)$$

$$2Co(IV) - (OH)BTC + C_6H_{12}O_6 \rightleftharpoons 2Co(III) - BTC + C_6H_{10}O_6 + 2H_2O \quad (8)$$

The Nyquist plots of NiCo-BTC, Ni-BTC and Co-BTC are depicted in Fig. 4b. It is worth noting that none of the plots of all samples showed a distinct semicircle, indicating an outstanding electron transfer process related to double capacitance. However, in low frequency region, the Warburg impedance of NiCo-BTC is significantly lower than that of the

corresponding Ni-BTC and Co-BTC. It is clearly demonstrating that the diverse metal sources can provide more exposed active sites to enhance the oxidation of glucose, which can enrich the diffusion of electrolyte ions to modified electrode surface.[34] Fig. 4c displays the CV curves of bimetallic MOF at 5-100 mV s^{-1}. As depicted in Fig. 4d, the anode peak current and the cathode peak current are linearly related to the square root of the scan rates, which illustrates the characteristic diffusion-controlled electrochemical process.[33] Fig. 4e shows the chronoamperometry curves of NiCo-BTC with various working voltage (0.3-0.55 V), which reveals the relationship between current response and applied potential. The highest response current of NiCo-BTC is obtained at 0.5 V (Fig. 4f), which is used as the operating voltage in the following measurements.

The i-t curves of as prepared MOFs with and without 0.1 mM glucose are displayed in S10 a-c. Fig. S10 d-f summarize the linear correlation between I_{cat} and corresponding $t^{-1/2}$. Diffusion coefficient (D) is a critical parameter for the electrocatalytic reaction of the electrode materials. It was acquired by Cottrell's equation, as shown in Eq (9).

$$I_{cat} = nFAD^{1/2}C_0\pi^{-1/2}t^{-1/2} \quad (9)$$

Where I_{cat} represents the current with 0.1 mM glucose, D means the diffusion coefficient (cm^2 s^{-1}), F denotes the Faraday's constant (C mol^{-1}), n indicates the number of electrons transferred (according to the Eqs (6), (7) and (8) n was equal to 1)[35,36], t displays the elapsed time (s), A stands for the electrode area (cm^2) and C_0 refers to the substrate concentration (mM). The D value of NiCo-BTC is 6.7×10^{-3} cm^2 s^{-1} (Fig. S8d), obviously higher than that of Co-BTC (1.8×10^{-3} cm^2 s^{-1}, Fig. S8e) and Ni-BTC (1.7×10^{-4} cm^2 s^{-1}, Fig. S8f). The higher value of D for NiCo-BTC means better capacity of diffusion. The excellent diffusion

capacity of NiCo-BTC results from the highly-opened nanosheet structure which can afford more contact sites.

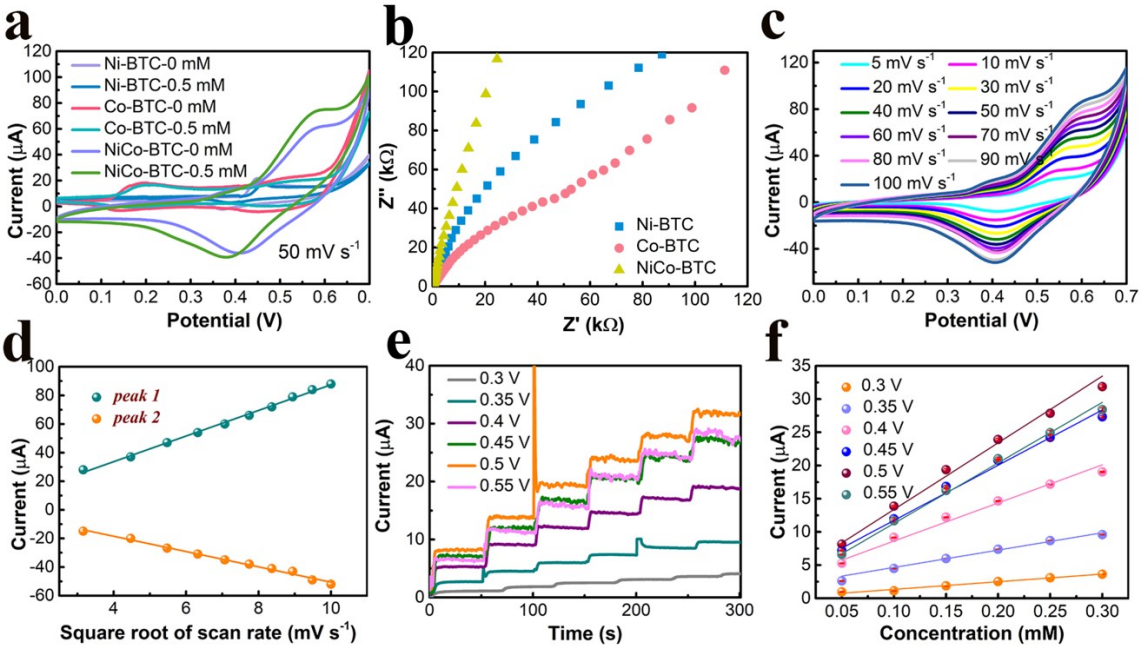

Fig. 4 (a) The CV curves of NiCo-BTC, Ni-BTC and Co-BTC with and without 0.5 mM glucose at the scan rate of 50 mV s^{-1}. (b) Nyquist plots of as prepared products. (c) The CV curves of NiCo-BTC at the different scan rates. (d) The calibration curves for square root of scan rate and corresponding current. (e) i-t curves of bimetallic MOF with different operating potential in 50 μM glucose. (f) The relationship between concentration and response current under different voltage.

The typical steady-state current response of as prepared samples at the optimal voltage is illustrated in Fig. 5a. All samples possess two or three linear ranges (Fig. 5b). The sensitivities, linear ranges and limit of detection (LOD) of all working electrodes are showed in Table S1. The NiCo-BTC obtained the high sensitivities of 1422.2 μA mM^{-1} cm^{-2} in low concentration region (5-205 μM) and 522.9 μA mM^{-1} cm^{-2} in high concentration region (205-2655 μM). The reason for the low sensitivity of materials in the high concentration range is due to excessive intermediate reactants blocking the active reaction site.[21] The sensitivities of

Ni-BTC (1219, 378.13 and 128 μA mM^{-1} cm^{-2}) and Co-BTC (207.4 and 80 μA mM^{-1} cm^{-2}) are clearly lower than those of NiCo-BTC in both linear regions. Furthermore, the lower limit of detection was obtained by NiCo-BTC (0.11 μM, signal/noise=3) which is obviously lower than that of Ni-BTC (0.98 μM) and Co-BTC (1.7 μM). The excellent response performance of bimetallic product for glucose can be assigned to the synergy between metal ions. Detailly, the competition between different metal ions leads to the formation of defects and unsaturated metal sites in the structure of MOFs. Defects in the structure not only facilitate the entry of target molecules but also provide more reaction sites. Unsaturated metal sites can be used as Lewis acid sites to participate in the catalytic reaction, which improves the catalytic performance. Moreover, the hybridization of metal ions increased the vacant d orbitals and the unpaired electrons, which results in the decrease of activation energy of electro-catalysis and further promotes redox of glucose molecules. Furthermore, as shown in the SEM images, the large adsorption sites were acquired by the highly-opened ultra-thin sheets structure. The interconnected sheets to form an array that effectively shortens the mass transfer path for glucose and intermediates. As shown in Table 1, the bimetallc electrode fabricated in this work possesses superior glucose detection performance compared with the previously studied literatures.

Table 1 Comparison of previous reported electrodes for nonenzymatic glucose sensing.

Materials	Linear ranges (μM)	Detection limit (μM)	Sensitivity (μA mM^{-1} cm^{-2})	References
3D hierarchical porous Co_3O_4	4-200 4000-12500	0.24	471.5 389.7	[37]
Ag NW[a] /NiCo LDH[b]	2-6000	0.66	71.42	[38]
UiO-67@Ni-MOF	5-3900	0.98	-	[39]

Cu-MOF/CNHs[c]	0.25-1200	0.078	-	[40]
Cu-BTC@SWCNT	0.2-80	0.00172	573	[41]
NiCo-MOF derivatives	0.5-4380	0.2	265.53	[42]
NCNT[d] MOF CoCu	50-2500	0.15	1027	[43]
NiCo-BTC	5-205	0.11	1422.2	This work
	205-2655		522.9	
	2655-5655		285.8	

[a] NW: nanowire.

[b] LDH: layered double hydroxide.

[c] CNHs: carbon nanohorns.

[d] NCNT: nitrogen-doped carbon nanotube.

3.3 Selectivity, repeatability, reproducibility and stability

There are various interfering substances during the detection of glucose in practical applications. Therefore, the chronoamperometry was employed to analysis the selectivity of fabricated bimetallic electrodes. It can be obviously seen from Fig. 5c, that all current responses of the interferences are less than 4.2%. In addition, 81.2% of the initial measured value is retained after the second addition of 30 μM glucose, demonstrating the excellent selectivity of bimetallic electrode. The excellent selectivity of NiCo-BTC can be ascribed to the electrostatic repulsion between the interfering substances and prepared samples. According to the reported literature, both Ni^{2+} and Co^{2+} possess the isoelectric points of 11.4.[44] Thus, NiCo bimetallic composites are negatively charged in alkaline environment. The central interferences are electronegative in an alkaline environment attributing to the absence of positively charged protons.[45] Therefore, the electrostatic repulsion between NiCo-BTC and interferences reduces the response current of the interfering substance, resulting in the increased selectivity of NiCo-BTC. Repeatability and productivity are also typical significance for the fabricated electrode. The relative standard deviation (RSD) of ten tests on same electrode is 5.2% (Fig. 5d). Five independent NiCo-BTC electrodes were also

experimented by the chronoamperometry in 30 μM glucose. The RSD of this test is less than 6.8% (Fig. 5e), manifesting the remarkable repeatability. Furthermore, chronoamperometry measurements were performed on the bimetallic electrodes every three days for one month. As depicted in Fig. 5f, the initial value of 80.02% can still be maintained after 30 days, showing good long-term stability of sensing performance.

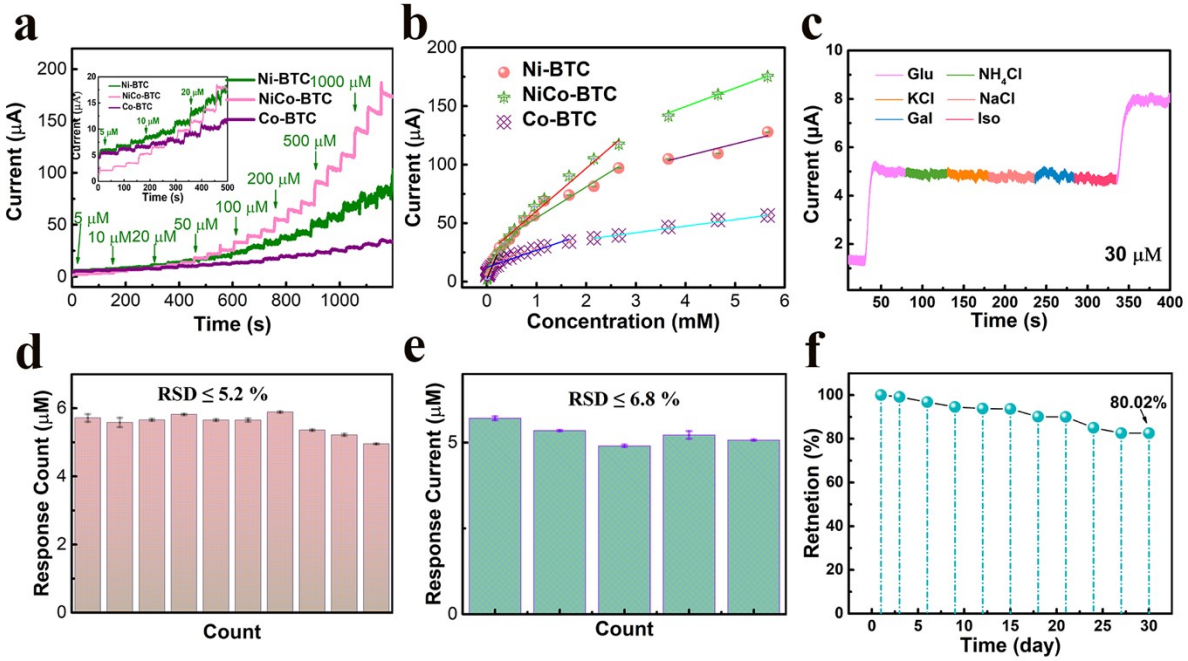

Fig. 5 (a) The current responses of samples with continuously dropping glucose; inset image is the current responses in low concentration. (b) The corresponding calibration curves of (a). (c) The current responses of NiCo-BTC with interfering species. (d) Ten tests of the same bimetallic electrode. (e) The current responses of five NiCo-BTC electrodes. (f) Long-term stability of bimetallic products.

3.4 Performance of MSC and wearable glucose sensor

Fig. 6a represents the CV results of the MSC from 10 to 500 mV s^{-1} in 0-1.6 V, which is sufficient for driving the glucose sensor. Fig. 6b depicts the GCD curves of the MSC in various current densities. The results of power and energy density calculated by GCD curves are shown in Fig. 6c. Obviously, the highest energy density (11.5 mWh cm^{-2}) is obtained at

the power density (0.26 mW cm^{-2}). In addition, the maximum power density (0.96 mW cm^{-2}) is also obtained, showing the excellent power performance of NiCo-BTC. As displayed in Fig. 6d, after 1000 cycles, the energy loss is only 15.4%, illustrating the upper long-term stability and maintenance-free characterization. The sensing performance of glucose sensors were analyzed by adding different concentration of glucose to the surface of the working area of the sensor at room temperature. The linear stepwise current responses curve is generated by the increased concentration of glucose (10 μM-200 μM), which indicates an ideal response curve of glucose sensors (Fig. 6e). The lowest LOD of prepared sensor for glucose is around 10 μM, indicating that the potential applications for personalized monitoring glucose level of as fabricated system.[46] Fig. 6f shows the corresponding calibration curve of the current responses results. The sensitivity calculated from the response consequence is 0.31 μA/μM. The remarkable sensitivity of the proposed device is mainly attributed to the structure and composition of ultra-thin electrode material. As for flexible ability of sensors, the CV curves of the prepared sensor have little difference at various bending angles, as depicted in Fig. 6g. Even when the bending angle reached 180 degrees, the loss of the original oxidation peak current is only 6.94%, demonstrating the significant flexibility of the glucose sensors (Figure 6h). The practical application of the wearable glucose sensor is displayed in the Fig. 6i. The real-time monitoring curves of sweat glucose is in accordance with the literature, indicating the potential application in personalized health monitoring.[47]

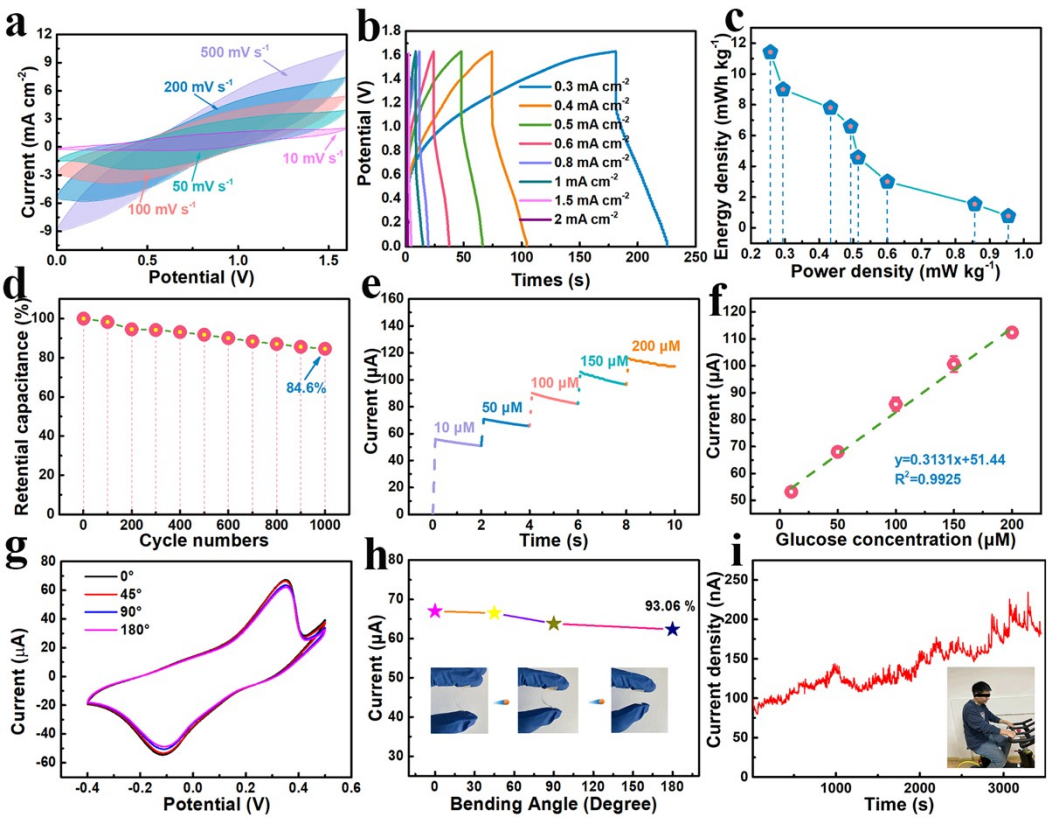

Fig. 6 (a) The CV curves of the power source device with various scan rates. (b) The GCD curves of the power equipment with different current densities. (c) The corresponding power and energy density of (b). (d) The long-term stability of as proposed MSC. (e) The current responses curves of the flexible glucose sensor. (f) The corresponding calibration curve of the current responses for (e). (g) The CV curves of glucose detector with different bending angle. (h) The corresponding redox peak current values of (g). (i) real-time monitoring curve of wearable sweat glucose sensor.

4. Conclusion

Overall, this research reports a three-dimensional nanoflower-like NiCo-BTC composed with two-dimensional ultrathin nanosheets. As prepared MOF electrode shows excellent electrochemical property with sensitivity of 1422.2 μA mM^{-1} cm^{-2}, good repeatability and excellent long-term stability for glucose detection. The MSCs based on the NiCo product

presents a high energy density (11.5 mWh cm^{-2}, at the power density of 0.26 mW cm^{-2}) and well long-term stability, which maintains the initial capacitance of 84.6% after 1000 cycles. The flexible wearable glucose biosensor was also triumphantly fabricated by magnetron sputtering process on the PET substrate. As designed glucose detector displays an ultra-high sensitivity of 0.31 μA/μM. The real-time sweat sensing consequence of the volunteer reveals that the sensor provides feasible adhibition in the field of noninvasive personal glucose monitoring.

CRediT authorship contribution statement

Xiaoting Zha: Conceptualization, Methodology, Supervision, Writing – review & editing. **Wenyao Yang:** Data curation, Formal analysis. **Liuwei Shi:** Writing-original draft. **Qi Zeng:** Formal analysis, Project administration. **Jianhua Xu:** Resources. **Yajie Yang:** Data curation Writing – review & editing.

Declaration of interests

The authors declare that they have no known competing financial interests or personal relationships that could have appeared to influence the work reported in this paper.

Acknowledgments

This work was supported by the National Natural Science Foundation of China (61971112 & 51907013). Science and Technology Research Program of Chongqing Municipal Education Commission (Nos. KJQN201901304, KJZD-K202201306 & HZ2021013).

References

1 A. Prabhakaran and P. Nayak, *ACS Appl. Nano Mater.*, 2020, **3**, 391–398.

2 X. Zhou, X. Gu, Z. Chen, Y. Wu, W. Xu and J. Bao, *Sensors and Actuators B: Chemical*,

2021, **329**, 129117.

3 Y. Khan, A. E. Ostfeld, C. M. Lochner, A. Pierre and A. C. Arias, *Adv. Mater.*, 2016, **28**, 4373–4395.

4 D. R. Walt, *ACS Nano*, 2009, **3**, 2876–2880.

5 H. Lee, Y. J. Hong, S. Baik, T. Hyeon and D. Kim, *Adv. Healthcare Mater.*, 2018, **7**, 1701150.

6 X. Zhu, Y. Ju, J. Chen, D. Liu and H. Liu, *ACS Sens.*, 2018, **3**, 1135–1141.

7 A. Chen and S. Chatterjee, *Chem. Soc. Rev.*, 2013, **42**, 5425.

8 C. Gao, Z. Guo, J.-H. Liu and X.-J. Huang, *Nanoscale*, 2012, **4**, 1948.

9 D. Jiang, Q. Liu, K. Wang, J. Qian, X. Dong, Z. Yang, X. Du and B. Qiu, *Biosensors and Bioelectronics*, 2014, **54**, 273–278.

10 W. Li, S. Lv, Y. Wang, L. Zhang and X. Cui, *Sensors and Actuators B: Chemical*, 2019, **281**, 652–658.

11 Y. Yan, Z. Shi, H. Li, L. Li, X. Yang, S. Li, H. Liang and Z. Qiao, *Chemical Engineering Journal*, 2022, **427**, 131604.

12 H. Li, L. Shi, C. Li, X. Fu, Q. Huang and B. Zhang, *ACS Appl. Mater. Interfaces*, 2020, **12**, 34095–34104.

13 X. Zha, Z. Wu, Z. Cheng, W. Yang, J. Li, Y. Chen, L. He, E. Zhou and Y. Yang, *Energy*, 2021, **220**, 119696.

14 S. Mallakpour, E. Nikkhoo and C. M. Hussain, *Coordination Chemistry Reviews*, 2022, **451**, 214262.

15 Y. Huo, M. Bu, Z. Ma, J. Sun, Y. Yan, K. Xiu, Z. Wang, N. Hu and Y.-F. Li, *Journal of*

Colloid and Interface Science, 2022, **607**, 2010–2018.

16 X. Cao, C. Tan, M. Sindoro and H. Zhang, *Chem. Soc. Rev.*, 2017, **46**, 2660–2677.

17 J. Duan, *Coordination Chemistry Reviews*.

18 Q. Li, Y. Liu, S. Niu, C. Li, C. Chen, Q. Liu and J. Huo, *Journal of Colloid and Interface Science*, 2021, **603**, 148–156.

19 J. Ding, L. Zhong, X. Wang, L. Chai, Y. Wang, M. Jiang, T.-T. Li, Y. Hu, J. Qian and S. Huang, *Sensors and Actuators B: Chemical*, 2020, **306**, 127551.

20 L. Zhang, C. Ye, X. Li, Y. Ding, H. Liang, G. Zhao and Y. Wang, *Nano-Micro Lett.*, 2018, **10**, 28.

21 D. Chen, L. Tian, C. Yin, Y. Liu, Q. Fu and C. Li, *Sensors and Actuators B: Chemical*, 2020, **323**, 128692.

22 T. Yang, L. Tian, E. Zhou, G. He, D. Chen and J. Xie, *Biosensors and Bioelectronics*, 2019, **143**, 111634.

23 S. Zhao, L. Zeng, G. Cheng, L. Yu and H. Zeng, *Chinese Chemical Letters*, 2019, **30**, 605–609.

24 M. Ezzati, S. Shahrokhian and H. Hosseini, *ACS Sustainable Chem. Eng.*, 2020, **8**, 14340–14352.

25 B. He, J.-J. Song, X.-Y. Li, C.-Y. Xu, Y.-B. Li, Y.-W. Tang, Q.-L. Hao, H.-K. Liu and Z. Su, *Nanoscale*, 2021, **13**, 810–818.

26 F. Israr, D. Chun, Y. Kim and D. K. Kim, *Ultrasonics Sonochemistry*, 2016, **31**, 93–101.

27 T. Zhao, H. Jiang and J. Ma, *Journal of Power Sources*, 2011, **196**, 860–864.

28 H.-M. Ma, J.-W. Yi, S. Li, C. Jiang, J.-H. Wei, Y.-P. Wu, J. Zhao and D.-S. Li, *Inorg.*

Chem., 2019, **58**, 9543–9547.

29 S. Li, C. Yu, J. Yang, C. Zhao, M. Zhang, H. Huang, Z. Liu, W. Guo and J. Qiu, *Energy Environ. Sci.*, 2017, **10**, 1958–1965.

30 T. Wang, S. Zhang, X. Yan, M. Lyu, L. Wang, J. Bell and H. Wang, *ACS Appl. Mater. Interfaces*, 2017, **9**, 15510–15524.

31 H. Rong, T. Chen, R. Shi, Y. Zhang and Z. Wang, *ACS Omega*, 2018, **3**, 5634–5642.

32 Z. Zhao, Y. Sun, J. Song, Y. Li, Y. Xie, H. Cui, W. Gong, J. Hu and Y. Chen, *Sensors and Actuators B: Chemical*, 2021, **326**, 128811.

33 H. Wei, Q. Xue, A. Li, T. Wan, Y. Huang, D. Cui, D. Pan, B. Dong, R. Wei, N. Naik and Z. Guo, *Sensors and Actuators B: Chemical*, 2021, **337**, 129687.

34 O. Adeniyi, N. Nwahara, D. Mwanza, T. Nyokong and P. Mashazi, *Sensors and Actuators B: Chemical*, 2021, **348**, 130723.

35 H. Xu, F. Han, C. Xia, S. Wang, S. Zhuiykov and G. Zheng, *Electrochimica Acta*, 2020, **331**, 135295.

36 G. Li, H. Huo and C. Xu, *J. Mater. Chem. A*, 2015, **3**, 4922–4930.

37 L. Han, D.-P. Yang and A. Liu, *Biosensors and Bioelectronics*, 2015, **63**, 145–152.

38 J. Xu, X. Qiao, M. Arsalan, N. Cheng, W. Cao, T. Yue, Q. Sheng and J. Zheng, *Journal of Electroanalytical Chemistry*, 2018, **823**, 315–321.

39 M. Lu, Y. Deng, Y. Li, T. Li, J. Xu, S.-W. Chen and J. Wang, *Analytica Chimica Acta*, 2020, **1110**, 35–43.

40 W. Zheng, Y. Liu, P. Yang, Y. Chen, J. Tao, J. Hu and P. Zhao, *Journal of Electroanalytical Chemistry*, 2020, **862**, 114018.

41 P. Arul, N. S. K. Gowthaman, S. A. John and M. Tominaga, *Electrochimica Acta*, 2020, **354**, 136673.

42 L. Wang, C. Hou, H. Yu, Q. Zhang, Y. Li and H. Wang, *ChemElectroChem*, 2020, **7**, 4446–4452.

43 S. eun Kim and A. Muthurasu, *Electroanalysis*, 2021, **33**, 1333–1345.

44 G. A. Parks, *Chem. Rev.*, 1965, **65**, 177–198.

45 Y. Ding, Y. Wang, L. Su, M. Bellagamba, H. Zhang and Y. Lei, *Biosensors and Bioelectronics*, 2010, **26**, 542–548.

46 Y. Lu, K. Jiang, D. Chen and G. Shen, *Nano Energy*, 2019, **58**, 624–632.

47 X. He, S. Yang, Q. Pei, Y. Song, C. Liu, T. Xu and X. Zhang, *ACS Sens.*, 2020, **5**, 1548–1554.